Supplementary Materials – Observation of Berry curvature in non-Hermitian system from far-field radiation

Xuefan Yin[1,2†], Ye Chen[2†], Xiaoyu Zhang[2], Zixuan Zhang[2], Susumu Noda[1], Chao Peng[2,3*]

[1] *Department of Electronic Science and Engineering, Kyoto University, Kyoto-Daigaku-Katsura, Nishikyo-ku, Kyoto 615-8510, Japan*

[2] *State Key Laboratory of Advanced Optical Communication Systems and Networks, School of Electronics, & Frontiers Science Center for Nano-optoelectronics, Peking University, Beijing, 100871, China*

[3] *Peng Cheng Laboratory, Shenzhen 518055, China*

1 Analytical theory of "bulk-radiation" correspondence

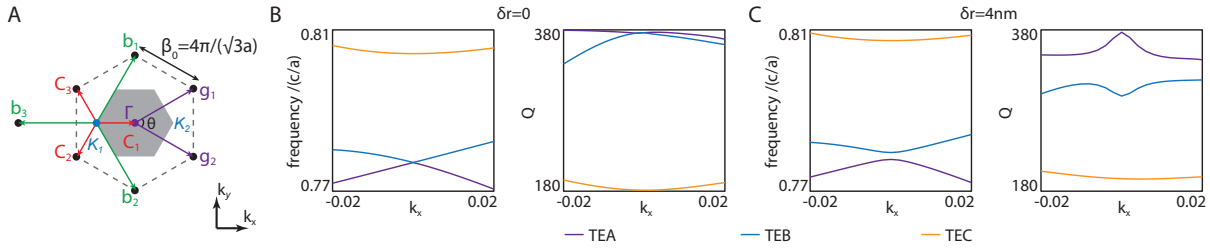

Figure S1: Reciprocal lattice and band structures of the PhC slab. (A) The reciprocal lattice of the PhC slab corresponds to Fig. 2 in the main-text. (B, C) The band structures of three band-edge modes near the $\mathcal{K}_1$ point for $\delta_r = 0$ nm and $\delta_r = 4$ nm, respectively.

In this section, we present the analytical theory of "bulk-radiation" correspondence from the coupled-wave theory (CWT) framework[1–3]. Without loss of generality, we consider a photonic crystal (PhC) slab shown in Fig. 2 in the main-text, whose reciprocal lattice is presented in Fig. S1A. The reciprocal vector is given by $\mathbf{G}_{sq} = s\mathbf{g}_1 + q\mathbf{g}_2$, where $\mathbf{g}_1 = \sin\theta\beta_0\hat{x} + \cos\theta\beta_0\hat{y}$, $\mathbf{g}_2 = \sin\theta\beta_0\hat{x} - \cos\theta\beta_0\hat{y}$ (purple vectors, Fig. S1) and $\beta_0 = 2\pi/a\sin(\theta)$ with θ denoting the angle between two basic reciprocal vector $\mathbf{g}_1$ and $\mathbf{g}_2$. Here we have $\theta = \pi/3$ for the honeycomb lattice. According to the Bloch theorem, the bulk modes in PhC slab can be expanded into a series of diffraction orders[2], denoted by indices (s, q):

$$E_{x,y}(x,y,z) = \sum_{sq} E^{sq}_{x,y}(z)e^{i(\mathbf{G}_{sq}-\mathbf{k}_{//})\mathbf{r}} = \sum_{mn} E^{mn}_{x,y}(z)e^{im\beta_0 x + in\beta_0 y}e^{-i\mathbf{k}_{//}\mathbf{r}} \tag{S1}$$

where $m = (s+q)\sin\theta$, $n = (s-q)\cos\theta$, and $\mathbf{k}_{//}$ is the in-plane Bloch vector related to the BZ center. For

quasi-transverse-electric (quasi-TE) modes, component Ez is relatively small and ruled by the transverse-field condition $\nabla \cdot [\varepsilon(\mathbf{r})\mathbf{E}(\mathbf{r})] = 0$, so that we treat it as the coupling route and consider only coupling equations of components E_x and E_y. Taking the $\mathcal{K}_1$ point as the offset center (blue dot, Fig. S1A), we denote $\mathbf{k}_{//} = -(k_x + 2\sin\theta/3)\beta_0\hat{x} - k_y\beta_0\hat{y}$, where $k_x\beta_0$ and $k_y\beta_0$ are the momentum displacements from the $\mathcal{K}_1$ point. For each diffraction order, the in-plane wavevector is given by $\beta_{sq} = \sqrt{(m + k_x + 2\sin\theta/3)^2 + (n + k_y)^2}\beta_0$.

According to the CWT, three diffraction orders dominate the modal energy in the vicinity of the second $\mathcal{K}_1$ point, denoted as the basic orders (b_{1-3}, green vectors, Fig. S1A), and three diffraction orders fall into the light cone and act as the radiation channels (C_{1-3}, red vectors, Fig. S1A). Other diffraction orders also exist but they have less energy and don't radiate, referred to as the high-order diffraction. By choosing the basic waves as the bases and taking into account all the possible couplings between them, we derive an eigenvalue problem as:

$$\lambda\psi = \hat{C}\psi \tag{S2}$$

in which the eigenvalue λ refers to the complex frequency of the bulk bloch modes and the eigenvector $\psi = [A_1,\ A_2,\ A_3]^T$ represents the amplitudes of basic orders. Generally, the coupling matrix $\hat{C}$ has a form of:

$$\hat{C} = \begin{bmatrix} a - \frac{2\xi}{\sqrt{3}}k_x & b & c \\ c & a + \frac{\xi}{\sqrt{3}}k_x - \xi k_y & b \\ b & c & a + \frac{\xi}{\sqrt{3}}k_x + \xi k_y \end{bmatrix} \tag{S3}$$

where ξ is a parameter determined from the PhC structure that depicts the band dispersion. Specifically, when the system preserves C_6 symmetry, we have $b = c$. In this case, the eigenvectors of matrix $\hat{C}$ at $\mathcal{K}_1$ point ($k_x = k_y = 0$) can be solved as:

$$\psi_1 = \begin{bmatrix} e^{-i\frac{\pi}{3}} \\ -1 \\ e^{i\frac{\pi}{3}} \end{bmatrix} \qquad \psi_2 = \begin{bmatrix} e^{-i\frac{\pi}{3}} \\ e^{i\frac{\pi}{3}} \\ -1 \end{bmatrix} \qquad \psi_3 = \begin{bmatrix} 1 \\ 1 \\ 1 \end{bmatrix} \tag{S4}$$

corresponding to the eigenvalues of:

$$\lambda_1 = a - e^{i\frac{\pi}{3}}b - e^{-i\frac{\pi}{3}}c \qquad \lambda_2 = a - e^{-i\frac{\pi}{3}}b - e^{i\frac{\pi}{3}}c \qquad \lambda_3 = a + b + c \tag{S5}$$

Here λ_1 and λ_2 correspond to $\mathrm{TE}_{A,B}$ modes, respectively. Readily find that if $b = c$ (C_6 symmetry), a degeneracy of λ_1 and λ_2 emerges at the $\mathcal{K}_1$ point (Fig. S1B). Once the C_6 symmetry is broken, the degeneracy lifts

to open a band gap (Fig. S1C). λ_3 refers to the separated TE_C mode. The coupling matrix $\hat{C}$ has included the couplings with TE_C mode. Then we apply a similarity transformation upon the matrix $\hat{C}$ to change the bases from basic diffraction orders to band-edge modes around second $\mathcal{K}_1$ point:

$$\begin{aligned}\hat{C}' &= \hat{M}\hat{C}\hat{M}^{-1} = [\psi_3\psi_2\psi_1]\hat{C}[\psi_3\psi_2\psi_1]^{-1} \\ &= \begin{bmatrix} a+b+c & -\frac{\sqrt{3}\xi}{3}(k_x - ik_y) & -\frac{\sqrt{3}\xi}{3}(k_x + ik_y) \\ -\frac{\sqrt{3}\xi}{3}(k_x + ik_y) & a - e^{-i\frac{\pi}{3}}c - e^{i\frac{\pi}{3}}b & -\frac{\sqrt{3}\xi}{3}(k_x - ik_y) \\ -\frac{\sqrt{3}\xi}{3}(k_x - ik_y) & -\frac{\sqrt{3}\xi}{3}(k_x + ik_y) & a - e^{-i\frac{\pi}{3}}b - e^{i\frac{\pi}{3}}c \end{bmatrix}\end{aligned} \tag{S6}$$

Accordingly, the eigenvectors of transformed matrix $\hat{C}'$ are $\hat{M}\psi_n$. The diagonal elements in $\hat{C}'$ are exactly the eigenvalues in Eq. S5, corresponding to three band-edge modes at $\mathcal{K}_1$: $\mathrm{TE}_{C,B,A}$; the off-diagonal terms represent the coupling strength between them. Note that the basis of $\hat{M}\psi_n$ is no longer the basic orders, but the band-edge modes $\mathrm{TE}_{C,B,A}$. Obviously, coupling matrix $\hat{C}'$ is exactly the Hamiltonian $\hat{H}$ describing the three-level system consisting of $\mathrm{TE}_{C,B,A}$ in the main-text. And the eigenvector $\hat{M}\psi_n$ actually represents the bloch mode u_n. For simplicity we denote the $\hat{M}\psi_n$ as u_n.

Accordingly, we derive the semi-analytical bulk Berry curvature as:

$$B_n = \sum_{m\neq n} \frac{\langle v_n|\nabla_{\mathbf{k}_{//}}\hat{C}'|u_m\rangle \times \langle v_m|\nabla_{\mathbf{k}_{//}}\hat{C}'|u_n\rangle}{(\lambda_n - \lambda_m)^2}, \qquad n, m \in \{A, B, C\} \tag{S7}$$

where $\langle v_n|$ is the left vector corresponding to right vector $|u_n\rangle$, defined as $\langle v_n|\hat{C}' = \lambda\langle v_n|$. By utilizing Eq. S3, S7 and S6, we can derive the bulk Berry curvature B_n presented in the main-text.

As we state in the main-text, the system can be treated as a quasi-degenerate two-level subsystem if the band gap between $\mathrm{TE}_{A,B}$ is sufficiently small to make the coupling from TE_C mode neglectable. To derive the two-level subsystem model, we derive a reduced coupling matrix between $\mathrm{TE}_{A,B}$ by removing the first row and the first column of $\hat{C}'$ which represent the coupling from TE_C mode:

$$\hat{C}_t = \begin{bmatrix} \lambda_1 & -\frac{\sqrt{3}\xi}{3}(k_x - ik_y) \\ -\frac{\sqrt{3}\xi}{3}(k_x + ik_y) & \lambda_2 \end{bmatrix} \tag{S8}$$

Accordingly, the reduced coupling matrix $\hat{C}_t$ is exactly the reduced Hamiltonian $\hat{H}_t$ in the main-text. The eigenvectors and eigenvalues of $\hat{C}_t$ can be derived as:

$$\begin{aligned}\lambda_{n;t} &= \frac{\Delta}{2} \pm \sqrt{\frac{\Delta^2 + 4\eta^2(k_x^2 + k_y^2)}{4}} \\ u_{n;t} &= [1, \quad \frac{\lambda_{n;t}}{\eta(k_x - ik_y)}]^T\end{aligned} \tag{S9}$$

where $\Delta = \lambda_2 - \lambda_1 = 2\delta$ and $\eta = -\sqrt{3}\xi/3$. When $\Delta = 0$, the eigenvectors turn to $[1, \pm|\eta|e^{i\theta_k}/\eta]$, where $e^{i\theta_k} = \sqrt{k_x^2 + k_y^2}/(k_x - ik_y)$, indicating a diabolic point (DP) residing right at the $\mathcal{K}_1$ point. By applying Eq. S8 and S9, we further derive the theoretical bulk Berry curvature and Berry phase as:

$$\begin{aligned} B_{n;t} &= \pm\frac{2\Delta\eta^2}{(\Delta^2 + 4\eta^2(k_x^2 + k_y^2))^{3/2}} \\ \gamma_{n;t} &= \pm\left(\pi - \frac{\Delta}{\sqrt{\Delta^2 + 4\eta^2(k_x^2 + k_y^2)}}\pi\right) \end{aligned} \tag{S10}$$

Eq. S10 is exactly the same with Eq. 3 and Eq. 4 in the main-text. We note that, compared to Eq. S7, Berry curvature and Berry phase in Eq. S10 are derived from the two-level subsystem (Eq. S8) without the contribution from TE_C.

As we stated in the main-text, we conclude $B_{n;t} \approx B_n$ when the coupling from TE_C is small enough to be neglected. Otherwise, they will deviate from each other as we presented in Fig. 5 in the main-text. On the other hand, the Berry curvature B_n or $B_{n;t}$ are complex numbers for non-Hermitian systems. According to Eq. S10, the complex values come from the complex band gap Δ with its imaginary part representing the leaky rate difference of $\mathrm{TE}_{A,B}$. However, compared with the real part that represents the frequency difference, its imaginary part is quite small. Hence, the imaginary part of Berry curvature is also small and can be neglected. Therefore, the non-Hermitian system in our experiment can be treated as the quasi-Hermitian system and thus we neglect the imaginary part in the main-text. We also emphasize that our method is also valid for general non-Hermitian systems where the imaginary part of Berry curvature is notably large.

Next, we discuss the far-field radiation and the radiation Berry curvature. As we stated, the radiations from bulk modes in PhC slab are exactly the diffraction orders residing inside the light cone. From the view of the CWT, for a radiative wave in channel q, the radiation vector is diffracted by the basic orders:

$$\Psi_{rad;n} = \begin{bmatrix} c_{s;n} \\ c_{p;n} \end{bmatrix} = \begin{bmatrix} d_1 & d_2 & d_3 \\ f_1 & f_2 & f_3 \end{bmatrix} \begin{bmatrix} A_{1;n} \\ A_{2;n} \\ A_{3;n} \end{bmatrix} = \hat{P}_{rad}\psi_n \tag{S11}$$

where $c_{s;n}$ and $c_{p;n}$ are radiation components in $s - p$ plane, perpendicular to the wavevector of channel q[4]. Here we omit the subscript q for simplicity. d_{1-3} and f_{1-3} are coupling terms between the basic orders ψ_n and the radiation components $c_{s;n}$ and $c_{p;n}$. The matrix $\hat{P}_{rad}$ is the projection matrix that describes such a radiation process.

However, in a realistic experiment, it is usually not easy to capture the polarization of radiation in $s-p$ plane when the emitting angle is relatively large. To address the problem, we project the components $c_{s;n}$ and $c_{p;n}$ to the $x-y-z$ coordinate system aligned with the experiment setup, and obtain three new components $c_{x;n}$, $c_{y;n}$ and $c_{z;n}$. Ruled by the transverse-field condition, the $c_{z;n}$ component is not independent. As a result, we can use $c_{x;n}$ and $c_{y;n}$ components to derive a new vector Ψ_n:

$$\Psi_n = \begin{bmatrix} c_{x;n} \\ c_{y;n} \end{bmatrix} = \hat{P}_{xy}^{sp}\Psi_{rad;n} = \hat{P}_{xy}^{sp}\hat{P}_{rad}\psi_n = \hat{P}\psi_n \tag{S12}$$

Obviously, the vector Ψ_n is just a projection of the original radiative vector $\Psi_{rad;n}$ in $x-y$ plane, described by projection matrix $\hat{P}_{xy}^{sp}$. Therefore, Ψ_n is also a projection of wavefunction ψ_n. In other words, the Ψ_n vector plays the same role as the original $\Psi_{rad;n}$ — the window to extract the underneath bulk topology. Moreover, singularities or vortexes upon $\Psi_{rad;n}$ would also be "projected" into Ψ_n. Considering Ψ_n is much easier to measure, we use Eq. S12 rather than Eq. S11 to derive the "bulk-radiation" correspondence, and observe the band topology through measuring Ψ_n in $x-y$ plane. Without losing generality, we denote Ψ_n as the radiative vector in the main-text, too.

For the three-level system including TE_C mode, no matter we employ $\Psi_{rad;n}$ or Ψ_n, the radiative vector is always a 2-dimensional one and thus the overall projection matrix $\hat{P}$ is a 2×3 one, indicating that a single channel can't capture the full information of the wavefunction. To get rid of the unnecessary mode TE_C, we rearrange the Eq. S12 as:

$$\Psi_n = \hat{P}\psi_n = \hat{P}\hat{M}^{-1}\hat{M}\psi_n = \hat{P}\hat{M}^{-1}u_n \tag{S13}$$

which indicates $\hat{P}^q\hat{M}^{-1}$ is the new projection matrix for the bulk modes u_n. If mode TE_C can be neglected, the first element of u_n and the first column of $\hat{P}\hat{M}^{-1}$ can be neglected, resulting in a reduced projection matrix $\hat{P}_t = \hat{P}\hat{M}^{-1}[:, 2:3]$ and two-dimentional eigenvector $u_{n;t} = u_n[2:3]$ for the two-level subsystem. In this way, we obtain a 2×2 matrix $\hat{P}_t$, representing a linear transformation between the bulk mode and the far-field radiation: $\Psi_{n;t} = \hat{P}_t u_{n;t}$.

Then we derive the "bulk-radiation" correspondence of the Berry curvature. As we stated in the main-text, assuming the far-field radiation is smooth, and the matrix $\hat{P}_t$ is invertible, we can apply similarity transformation by employing the matrices $\hat{P}_t$ and $[\hat{P}_t]^{-1}$:

$$\hat{C}_t^r = \hat{P}_t\hat{C}_t[\hat{P}_t]^{-1} \tag{S14}$$

The radiative vector $\Psi_{n;t}$ is exactly the eigen vector of the new Hamiltonian $\hat{C}_t^r$, with the left vector of $\langle\Phi_{n;t}| = \langle v_{n;t}|[\hat{P}_t]^{-1}$ where $\langle v_{n;t}|$ is the left vector corresponding to $|u_{n;t}\rangle$, obeying the bi-orthogonal condition of $\langle\Phi_{m;t}|\Psi_{n;t}\rangle = \langle v_{m;t}|u_{n;t}\rangle = \delta_{mn}$. By applying the new bi-orthogonal bases for Hamiltonian $\hat{C}_t^r$, we can derive the radiation Berry curvature as

$$\begin{aligned} B_{n;t}^r &= i\nabla_{\mathbf{k}_{/\!/}} \times \langle\Phi_{n;t}|\nabla_{\mathbf{k}_{/\!/}}\Psi_{n;t}\rangle \\ &= i\nabla_{\mathbf{k}_{/\!/}} \times \langle v_{n;t}|[\hat{P}_t]^{-1}\nabla_{\mathbf{k}_{/\!/}}\hat{P}_t|u_{n;t}\rangle + i\nabla_{\mathbf{k}_{/\!/}} \times \langle v_{n;t}|[\hat{P}_t]^{-1}\hat{P}_t|\nabla_{\mathbf{k}_{/\!/}}u_{n;t}\rangle \end{aligned} \tag{S15}$$

Eq. S15 indicates the radiation Berry curvature defined in far-field bases $\langle\Phi_{n;t}|$ and $|\Psi_{n;t}\rangle$ consists of two parts: the first term comes from the projection operator $\hat{P}_t$; the second term is exactly the bulk Berry curvature defined in wavefunctions $|u_{n;t}\rangle$ and $\langle v_{n;t}|$, representing the topology of the bulk band. As we stated in the main-text, once the projection matrix is smooth without amplitude vortexes, the first term in Eq. S15 vanishes, and we have $B_{n;t}^r \approx B_{n,t}$, namely that the radiation Berry curvature directly corresponds to the band topology in the two-level system — the "bulk-radiation" correspondence we described in the main-text.

In summary, to succeed in extracting the band topology from the radiation channel, the bulk-radiation correspondence can be derived as:

$$B_n \approx B_{n;t} \approx B_{n;t}^r \tag{S16}$$

The first term B_n is the bulk Berry curvature defined in the original multi-level system (three levels in our system). The last term $B_{n;t}^r$ is the radiation Berry curvature which can be directly measured from far-field polarization. The bulk-radiation correspondence in Eq. S16 relies on two premises. First, the system should be a two-level system to allow $B_n \approx B_{n;t}$. In the case that the coupling from TE_C mode can't be neglected, Eq. S8 can't describe the physics of the original system and $B_{n;t}$ deviates from original B_n, indicating that we cannot retrieve sufficient information from a single radiation channel to represent the band topology. Second, the radiation channel should be smooth to allow $B_{n;t}^r \approx B_{n;t}$. If the projection process itself owns nontrivial geometry, for instance, the amplitude vortexes in the momentum space, the first term in Eq. S15 doesn't vanish, and thus $B_{n;t}^r \neq B_{n;t}$. As a result, some extra phases would be added to the band topology, because the radiation Berry curvature is actually an overlapping of the band topology and channel geometry. Readily check that our PhC system fulfills the aforementioned premises. In the next sections, we would present some examples to show how extra amplitude vortexes ruin the "bulk-radiation" correspondence, and discuss how to retrieve the bulk topology from the polarization in multi-level systems.

2 Projection matrix with amplitude vortex

As we stated in the last section, the premise of the bulk-radiation correspondence (Eq. S16) is that the far-field radiation is smooth so that the projection matrix $\hat{P}_t$ can be inverted. According to Eq. S15, poor-defined $[\hat{P}_t]^{-1}$ and nontrivial $\nabla\hat{P}_t$ contribute to the first term in $B^r_{n;t}$, making it deviated from the bulk topology $B_{n;t}$. In this section, we propose an example to see how nontrivial geometry of the radiation channel itself affects the measurement of the bulk Berry curvature from the far field.

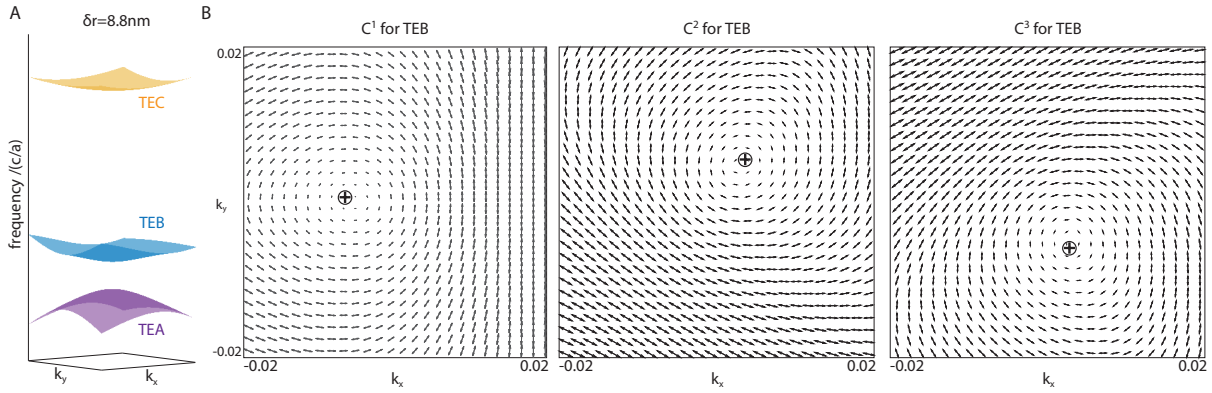

Figure S2: PhC slab with polarization defects as the amplitude vortexes in radiation channels. (A) band structures of the free-standing honeycomb-latticed PhC slab around the second $\mathcal{K}_1$ point. The slab thickness $h = 1.067a$; the radii of two air holes in unit cell are $r_1 = 0.12a$ and $r_2 = 0.14a$, respectively. (B) Polarization vector fields of three channels C_{1-3} for TE_B mode. Polarization defects carrying integer topological charge can be found in every channel, symmetric with each other under the C_3 symmetry.

One type of non-trivial radiation geometry is the amplitude vortexes, where the amplitude of radiation vanishes and thus prevents the radiation channel from delivering the bulk band information out. Similar to the main-text, we consider a free-standing PhC slab with a honeycomb lattice of different parameters. Here the slab thickness is set to be $h = 1.067a$, and the radii of two holes in the unit cell are $r_1 = 0.12a$ and $r_2 = 0.14a$, respectively. If we consider the same lattice constant with the main-text, that is $a = 440$ nm, the $\delta_r = 8.8$ nm. The band structures around the second $\mathcal{K}_1$ point are shown in Fig. S2A.

We still focus on the two-level system: TE_A (purple sheet) and TE_B (blue sheet). One can check that there are no polarization defects in all the three channels C_{1-3} for TE_A mode. In other words, for TE_A, the far-field radiation is smooth. However, as shown in Fig. S2B, a polarization defect with vanishing amplitude emerges in every channel for TE_B mode, carrying an integer topological charge of $q = +1$. Around these

polarization defects, the far-field radiation is not smooth but poorly defined. Note that since the PhC slab is protected by the C_3 symmetry, three polarization defects in three channels are symmetric with each other with respect to the $\mathcal{K}_1$ point.

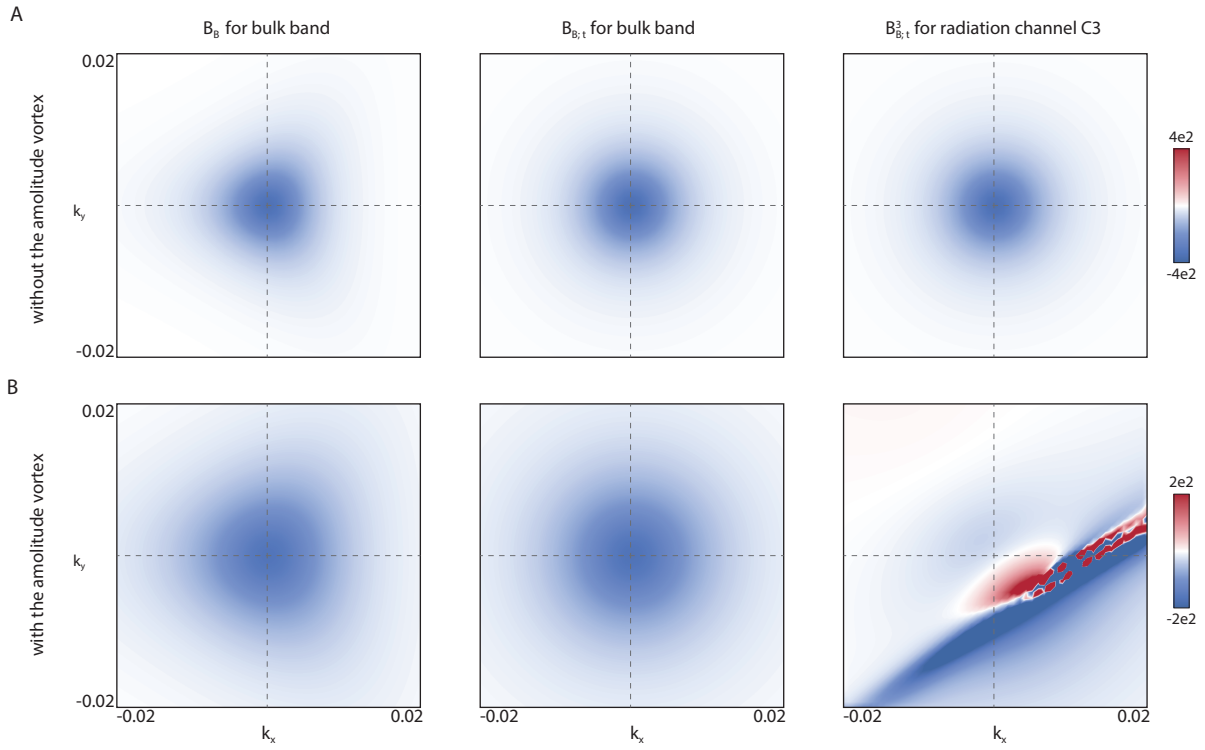

Figure S3: Bulk/radiation Berry curvatures without/with amplitude vortexes. (A) For the case without the amplitude vortexes (reproduced from Fig. 4 in the main-text), bulk Berry curvatures for rigorous three-level system (left panel), reduced two-level subsystem (middle panel), and radiation Berry curvature measured from channel C_3 (right panel). (B) For the case with the amplitude vortexes (case in Fig. S2), bulk band Berry curvatures for rigorous three-level system (left panel), reduced two-level subsystem (middle panel), and radiation Berry curvature measured from channel C_3 (right panel).

Then we investigate how these amplitude vortexes ruin the bulk-radiation correspondence. Specifically, we take channel C_3 as an example and calculate B_B, $B_{B;t}$ and $B^3_{B;t}$ of TE_B mode with (case in Fig. S2) and without (case in Fig. 4 in the main-text, $\delta r = 7$nm) the amplitude vortexes, respectively. B_B is the bulk Berry curvature in the original three-level system (Eq. S7); $B_{B;t}$ is the bulk Berry curvature in two-level subsystem which excludes the coupling from TE_C (Eq. S10); $B^3_{B;t}$ is the radiation Berry curvature from channel C_3 (Eq. S15). The results are shown in Fig. S3. Obviously, similar with the main-text, without

the amplitude vortexes, all three types of Berry curvatures are well-defined, and almost the same with each other, validating the bulk-radiation correspondence we derive in Eq. S16. We emphasize that, the agreement between B_B and $B_{B;t}$ conceives that the coupling from TE_C can be neglected. However, as shown in Fig. S3B, when a polarization defect emerges in the channel C_3, radiation Berry curvature $B^3_{B;t}$ is remarkably different from the other two ones, and a singularity appears in $B^3_{B;t}$, right at the location of the defect, indicating the amplitude vortex brings extra phases to $B^3_{B,t}$ and destroys the bulk-radiation correspondence.

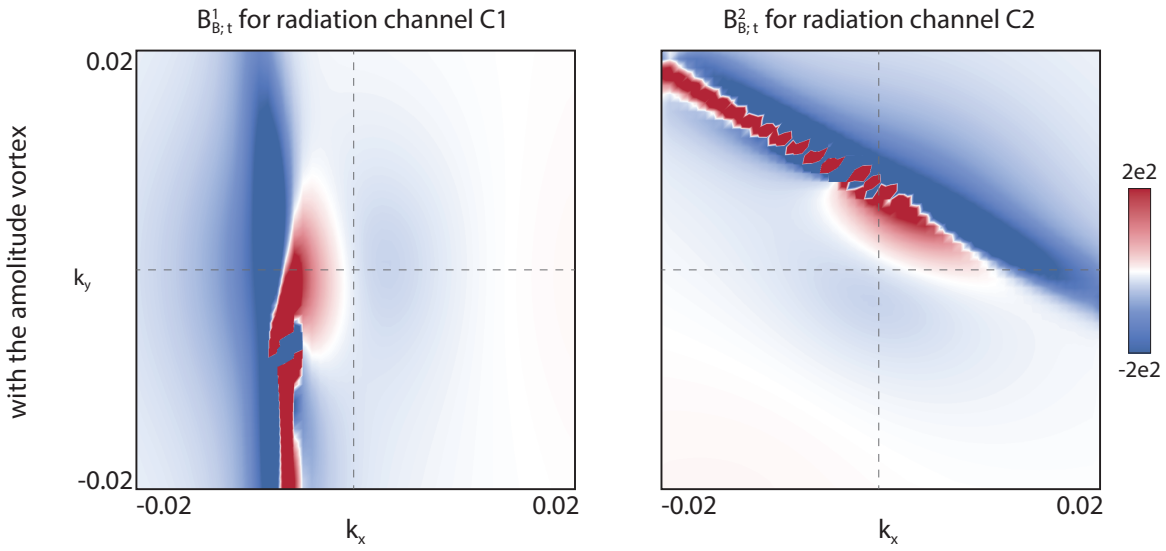

Figure S4: Radiation Berry curvatures with amplitude vortexes measured from channel C_1 (left panel) and C_2 (right panel).

Similar things happen in the other two radiation channels. As shown in Fig. S4, singularities emerge in the radiation Berry curvatures $B^{1,2}_{B;t}$, right at the location of polarization defects in radiation channel $\mathrm{C}_{1,2}$. This indicates that the singularities in $B^r_{n;t}$ are exactly the result of the amplitude vortexes in far-field radiation. Therefore, to retain the bulk-radiation correspondence, we must make sure that the $\hat{P}_t$ is well-defined everywhere inside the region of interest.

3 Physics and observation of left vector $\langle\Phi(\mathbf{k}_{/\!/})|$

The observation of radiation Berry curvature in a non-Hermitian system requires both the right radiative vector $|\Psi(\mathbf{k}_{/\!/})\rangle$ and the left radiative vector $\langle\Phi(\mathbf{k}_{/\!/})|$. The right vector $|\Psi(\mathbf{k}_{/\!/})\rangle$ directly corresponds to the polarization, which can be easily measured. However, the physics of left vector $\langle\Phi(\mathbf{k}_{/\!/})|$ is not quite straightforward. For simplicity, we solve the left vector from the orthogonality condition $\langle\Phi_m(\mathbf{k}_{/\!/})|\Psi_n(\mathbf{k}_{/\!/})\rangle = \delta_{mn}$ in the main-text. Here we emphasize that the left vector can also be directly measured. We start with the wave equation in a PhC slab[5]:

$$\nabla \cdot (\nabla \cdot \mathbf{E}) - \nabla^2 \mathbf{E} = k_0^2 \varepsilon(r)\mathbf{E} \tag{S17}$$

The eigenvalue problem can be arranged as $\hat{H}\mathbf{E} = \lambda\varepsilon(r)\mathbf{E}$, in which $\hat{H}$ is the Hamiltonian. According to the Bloch theorem, we have $\mathbf{E} = E_{\mathbf{k}_{/\!/}} e^{-i\mathbf{k}_{/\!/}\cdot\mathbf{r}}$, and $E_{\mathbf{k}_{/\!/}}$ is the eigen function of the unit-cell Hamiltonian $\hat{H}_k = e^{i\mathbf{k}_{/\!/}\mathbf{r}}\hat{H}e^{-i\mathbf{k}_{/\!/}\mathbf{r}}$. According to time-reversal symmetry, we have[6]

$$\hat{H}_{-\mathbf{k}_{/\!/}} = \hat{H}^*_{\mathbf{k}_{/\!/}} \tag{S18}$$

Then we discuss the relationship between bulk modes at $\mathbf{k}_{/\!/}$ and $-\mathbf{k}_{/\!/}$ under the CWT framework. As we stated in the last section, we can decompose the wavefunction $E_{\mathbf{k}_{/\!/}}$ into a series of diffraction orders $E_{x,y;sq}e^{i(\mathbf{G}_{sq}-\mathbf{k}_{/\!/})\mathbf{r}}$ (see Eq. S1), then we truncate the diffraction orders: we only keep the basic orders and treat other orders as the coupling paths. The basic orders are governed by the coupling matrix $\hat{C}$ (Eq. S3), which is a sub-matrix of original Hamiltonian $\hat{H}_{\mathbf{k}_{/\!/}}$. And hence, the time-reversal counterpart of $\hat{C}$ is:

$$\mathcal{T}[\hat{C}(\mathbf{k}_{/\!/})] = \hat{S}^{-1}\hat{C}^{\dagger}(\mathbf{k}_{/\!/})\hat{S} \tag{S19}$$

where $\hat{S}$ is a unitary matrix labeling the sequence of basic orders. According to Eq. S18, we also obtain another equation:

$$\mathcal{T}[\hat{C}(\mathbf{k}_{/\!/})] = \hat{C}^{*}(-\mathbf{k}_{/\!/}) \tag{S20}$$

Combining Eq. S19 and Eq. S20, we derive:

$$\hat{C}(-\mathbf{k}_{/\!/}) = \hat{S}^{-1}\hat{C}^{T}(\mathbf{k}_{/\!/})\hat{S} \tag{S21}$$

Eq. S21 depicts the **reciprocity** of coupling matrix $\hat{C}$, indicating that eigenvalues at $\mathbf{k}_{/\!/}$ point and $-\mathbf{k}_{/\!/}$ point are the same, regardless of whether the system preserves the C_2 symmetry or not.

In fact, the reciprocity is a consequence of the time-reversal symmetry in a general non-Hermitian PhC slab. As we stated, the original Hamiltonian $\hat{H}_{\mathbf{k}_{/\!/}}$ has the time-reversal symmetry to guarantee energy conservation. However, for an open PhC slab, the matrix $\hat{C}$ is just a sub-matrix of $\hat{H}_{\mathbf{k}_{/\!/}}$ and describes the coupling between basic orders and how they couple to the radiative channels that lose energy out of the slab. Therefore, $\hat{C}$ is a non-Hermitian matrix with complex eigenvalue λ, whose imaginary part exactly describes how energy flows out of the slab as the radiation. Considering a time-reversal version of the radiation process, the energy should flow back from outer space into the slab, characterized by λ^*, which is exactly the eigenvalue of $\hat{S}^{-1}\hat{C}^{\dagger}(\mathbf{k}_{/\!/})\hat{S}$ in Eq. S19. Such a time-reversal process is not physical and thus we conclude $\hat{C}$ directly possesses the reciprocity rather than the time-reversal symmetry. After a similar transformation, coupling matrix $\hat{C}'$ in Eq. S6 also obtains the reciprocity rather than the time-reversal symmetry.

Further, we consider the left vectors. The bi-orthogonal bases of $\hat{C}$ are defined as follows:

$$\begin{aligned} \hat{C}(\mathbf{k}_{/\!/})|\psi(\mathbf{k}_{/\!/})\rangle &= \lambda(\mathbf{k}_{/\!/})|\psi(\mathbf{k}_{/\!/})\rangle \\ \langle\phi(\mathbf{k}_{/\!/})|\hat{C}(\mathbf{k}_{/\!/}) &= \lambda(\mathbf{k}_{/\!/})\langle\phi(\mathbf{k}_{/\!/})| \end{aligned} \tag{S22}$$

From Eq. S19, we find the vector $\hat{S}^{-1}|\phi(\mathbf{k}_{/\!/})\rangle$ is exactly the eigenvector (right vector) of $\mathcal{T}[\hat{C}(\mathbf{k}_{/\!/})]$, where $|\phi(\mathbf{k}_{/\!/})\rangle$ denotes the adjoint of left vector $\langle\phi(\mathbf{k}_{/\!/})|$. Namely, the adjoint of left vector corresponds to the "right vector" of the time-reversal system. This is the physical meaning of the left vectors.

As we stated before, in time-reversal system, the energy would flow back from outer-space to the slab. In fact, for the specific two-level system, the energy would flow backward through exactly the same channel with the one where it leaks outward. To present this, recall the projection matrix $\hat{P}$ that connects the original right vector $|\psi(\mathbf{k}_{/\!/})\rangle$ and the radiative vector as $|\Psi(\mathbf{k}_{/\!/})\rangle = \hat{P}|\psi(\mathbf{k}_{/\!/})\rangle$. For reduced two-level system, we also have $|\Psi_t(\mathbf{k}_{/\!/})\rangle = \hat{P}_t|u_t(\mathbf{k}_{/\!/})\rangle$ (Eq. S13). Since the projection matrix $\hat{P}_t$ is invertible, in the time-reversal process, the energy flows back through the exactly same channel, described by $[\hat{P}_t]^{-1}$. This process corresponds to the left vector $\langle\Phi_t(\mathbf{k}_{/\!/})| = \langle v_t(\mathbf{k}_{/\!/})|[\hat{P}_t]^{-1}$.

Further, we can apply the reciprocity relationship in Eq. S21 to make the left vector directly observable. Specifically, we derive:

$$\langle\Phi_t(\mathbf{k}_{/\!/})| = (|\Psi_t(-\mathbf{k}_{/\!/})\rangle)^T \left[\hat{P}_t^T(\mathbf{k}_{/\!/})\right]^{-1} \hat{S}\,\hat{P}_t^{-1}(-\mathbf{k}_{/\!/}) \tag{S23}$$

which indicates that the left vector $\langle\Phi|$ in $\mathbf{k}_{/\!/}$ point can be connected to the right vector $|\Psi\rangle$ in $-\mathbf{k}_{/\!/}$ point, while the latter can be directly measured. In main-text, we neglect the unitary matrix $\hat{S}$ for simplicity.

4 Probing of bulk band topology from far-field observables

In the main-text, we employ polarization measurements to realize the bulk topology tomography. In fact, despite of the polarization, there are some other attributes of the radiation that can be utilized to probe the bulk topology in principle, such as frequency and Q-factor. In this section, we discuss how to reconstruct the Hamiltonian through utilizing these observables, to claim that, for the far-field measurement of the Berry curvature in multi-level vector system, the polarization is indeed necessary.

We consider a non-Hermitian system with internal degree of freedoms (DOFs) of N, described by a Hamiltonian $\hat{H}$ represented as a $N \times N$ matrix. Considering the general case without any symmetry, there are N^2 unknown elements in all. This Hamiltonian can be fully determined by its eigenvalues and eigenvectors as:

$$\hat{H}|u_n\rangle = \lambda_n|u_n\rangle \qquad \langle v_n|\hat{H} = \lambda_n\langle v_n| \tag{S24}$$

Specifically, the elements in all the left vectors and right vectors are $2N^2$, and there are N eigenvalues by general. In all, there are $2N^2+N$ complex numbers. Notice that these elements are not independent. First, the bi-orthogonal conditions $\langle v_m|u_n\rangle = \delta_{mn}$ contributes to N^2 DOFs. Moreover, each right vector can be gauged with an arbitrary phase factor, giving rise to N DOFs. As a result, the number of independent elements in all the eigenvalues and eigenvectors is $2N^2 + N - N^2 - N = N^2$, which is exactly the number of DOFs that the original Hamiltonian requires. In other words, if we can measure **both the eigenvalues and eigenvectors**, we can reconstruct the Hamiltonian accordingly. One exception is the scalar single-valuable system with only one DOF, where eigenvalue has already presented all the information of the system.

In realistic photonic systems such as PhC slabs, the eigenvalues of the Hamiltonian refers to the complex frequencies of bulk Bloch modes, namely the frequencies and Q-factors, which can be in principle measured from the far field. However, we found that the Q-factors are particularly difficult to measure in practical samples, because many factors such as random scatterings, background noise, etc. would make the measurement inaccurate. Even if we can successfully obtain the eigenvalues, as we discussed above, it's still not enough to extract the bulk band topology of multi-level vector system since the complex frequencies don't contain any information about the wavefunctions.

However, the direct measurement of the eigenvectors is too challenging in practice because we need to measure the real-space wavefunctions, namely the electromagnetic wave distributions in the near field. Therefore, we conclude that to reconstruct the Hamiltonian, other observables associated with the wavefunction

are necessary. We propose that, polarization is a good candidate. According to the CWT framework (Eq. S11 and Eq. S12), polarization can be understood as the projection of wavefunctions in the far field. Therefore, they by nature carry the information of wavefunctions. In fact, since we focus on the measurement of the Berry curvature, which can only depend on the wavefunction ($B = i\nabla \times \langle\phi|\nabla\psi\rangle$), it's not necessary to reconstruct the original Hamiltonian, and we can solve the Berry curvature only from the polarization without the information of complex frequencies.

Next, we discuss how to retrieve the bulk topology from the far-field polarization in a general system with internal DOFs of N. We rearrange Eq. S12 for the nth band ($n \in (1, N)$) as:

$$\sum_{m=1}^{N}(d_m - \kappa f_m)A_{m;n} = 0 \tag{S25}$$

where $\kappa = c_{x;n}/c_{y;n}$ is the gauge-invariant radiation coefficient that represents the polarization. For x-polarized state, we can use $\kappa = c_{y;n}/c_{x;n}$ to avoid ill-definition. Note that the coefficients d_m and f_m can be derived from structural geometries by using the CWT, and κ can be directly measured. Obviously, each radiation channel can provide an equation like Eq. S25.

However, Eq. S25 only provides one DOF. To solve the right vector which contains N unknown elements, it seems that N channels are necessary to give N linearly independent equations like Eq. S25 to fully capture the wavefunction. Nevertheless, notice that the wavefunction can be gauged to an arbitrary phase and scaled in arbitrary amplitude, which reduces the required DOFs by one. For example, we can fix one of the elements (i.e. the first coefficient $A_{1;n}$) in $|u_n\rangle$ to 1, and thus Eq. S25 turns into:

$$\sum_{m=2}^{N}(d_m - \kappa f_m)A_{m;n} = -(d_1 - \kappa f_1) \tag{S26}$$

Accordingly, the number of unknown elements is reduced to $N - 1$, showing that the necessary number of linearly independent channels is $N - 1$. Specifically, for a two-level system with $N = 2$, observing only one radiation channel is enough to characterize the band topology, as we stated in the main-text.

There are two methods to obtain the left vectors. First, as we employed in the main-text, we can apply the bi-orthogonality condition to determine the left vectors after we observe all the right vectors. However, this method is not applicable when the number of internal DOFs N is very large. Instead, if only one bulk band is interested, we can adopt the second method that measures the left vectors from their time-reversal counterparts according to Eq. S23.

5 Observation of band topology in multi-level system

In this section, we present an example to explicitly show how to extract the band topology from far-field polarization in multi-level systems ($N > 2$).

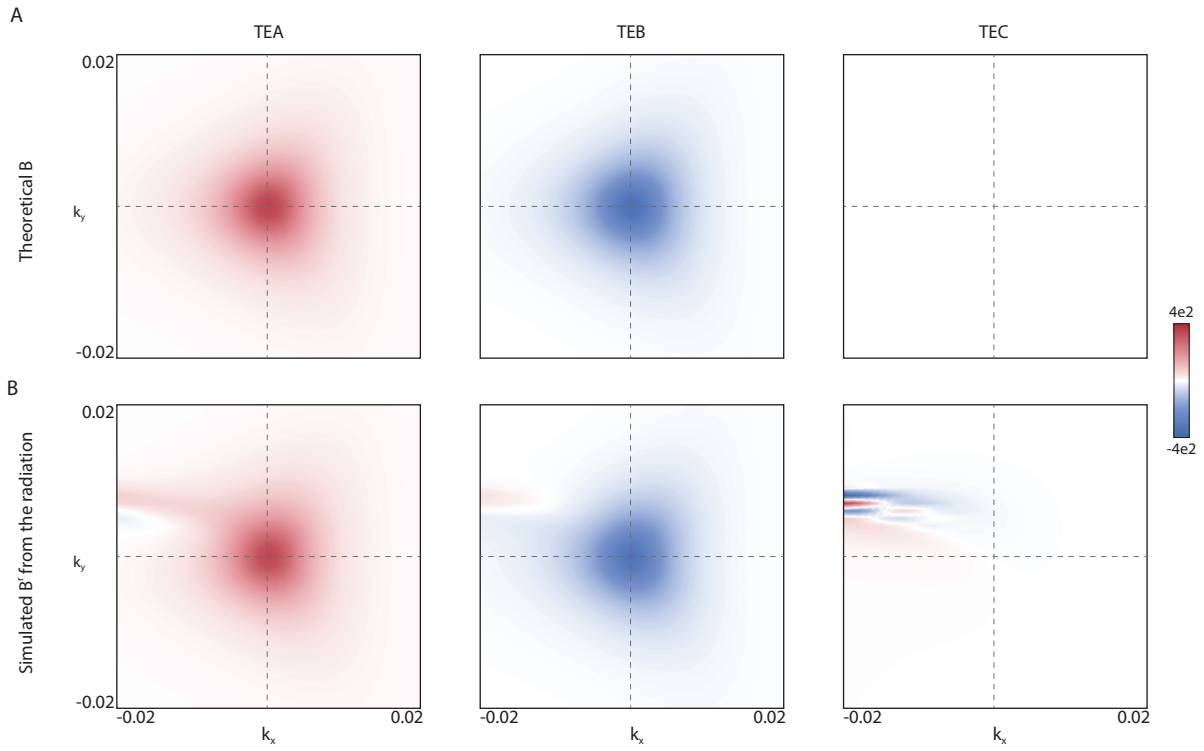

Figure S5: Bulk Berry curvature (A) and simulated radiation Berry curvature (B) for three-level system.

As shown in Fig. S5, we consider the three-level system in the main-text including the TE_C mode, and employ the method presented in last section to retrieve the Berry curvature from the radiation of all three bulk modes. The parameters of the PhC slab are the same as the Fig. 4 in the main-text with $\delta_r = 7$ nm. Specifically, according to Eq. S26, for a system of $N = 3$, two independent radiation channels are necessary to capture all the information of the wavefunctions. As we stated, around the second $\mathcal{K}_1$ point, there are three radiative channels $\mathrm{C}_{1,2,3}$. Therefore, we have enough DOFs to measure the bulk topology through the radiation.

Here we choose C_2 and C_3 channels and calculate the polarization distribution numerically for all three bands around the $\mathcal{K}_1$ point. Further, from Eq. S26, we solve the right vectors and left vectors accordingly derived from the bi-orthogonal condition. Finally, we derive the radiation Berry curvature for all the three

modes (Fig. S5B). As a comparison, we theoretically calculate the bulk Berry curvatures according to Eq. S7 (Fig. S5A). The two results agree well with each other, showing that even for the three-level system, our method is still valid.

In the main-text, we ignore the TE_C mode. Here, we quantitatively show that the exclusion of TE_C mode is reasonable, by comparing the geometric phases derived from the bulk Berry curvature of the three-level system and reduced two-level subsystem. Specifically, we take the TE_B mode as an example. We first apply the integral over the theoretical bulk Berry curvature B_B of the three-level system in Fig. S5B to derive the $\gamma_B = -0.6925\pi$. Then, according to Fig. S3, we derive the theoretical $\gamma_{B;t}$ for the reduced two-level subsystem as $\gamma_{B;t} = -0.7463\pi$, slightly smaller than γ_B (Fig. 5C in the main-text). By excluding the coupling from TE_C, the error of the Berry phase is about 8%, which is very small, proving that TE_C mode can be omitted in principle.

Next, we calculate the geometric phase from the radiation Berry curvature. We first derive the γ_B^r for the three-level system according to B_B^r in Fig. S5B as $\gamma_B^r = -0.6898$, which is very close to the γ_B, indicating that for the three-level system, the far-field polarization can completely present the topology of the wave-function. Then, we derive the $\gamma_{B;t}^3$ for two-level subsystem from the radiation channel C_3 as $\gamma_{B;t}^3 = -0.8359\pi$, which deviates from γ_B and γ_B^r with error of about 20.7%. As shown in Fig. 5C in the main-text, we have $\gamma_{B;t}^3 < \gamma_{B;t} < \gamma_B \approx \gamma_B^r$. When δ_r is relatively large, the exclusion of TE_C mode would result in a larger deviation in the radiation geometric phase γ_B^r than the bulk geometric phase γ_B. This is because TE_C also contributes to the far-field radiation.

Indeed with the TE_C band included, we can obtain more accurate results. However, we need to apply polarimetry measurements in two channels for all the three bands. As a comparison, once we exclude the TE_C band, we only have to measure one channel for two bands. For the case with relatively small δ_r, i.e. $\delta_r = 2$ nm, we obtain $\gamma_{B;t}^3 = -0.9507\pi$ which is very close to the theoretical $\gamma_B = -0.9034\pi$ (error of 5%). Therefore, when δ_r is small, it's acceptable to omit the TE_C mode to reduce the experimental complexity. Oppositely, when δ_r becomes larger (i.e. $\delta_r > 7$nm), serious deviation between $\gamma_{n,t}^r$ and γ_n leads to low reliability of the observation.

6 Radiation geometry and the "right-right" curvature

The radiation Berry curvature we discussed depends on both left and right vectors, referred as to the "left-right" curvature [7]. According to "Bulk-radiation correspondence", although this "left-right" curvature is defined by radiative vectors, it corresponds to the bulk band topology, but doesn't describe the geometry of the radiation itself. In fact, it's another type of Berry curvature which depends only upon the right radiation vector who describes the radiation geometry, denoted as the "right-right" curvature [7].

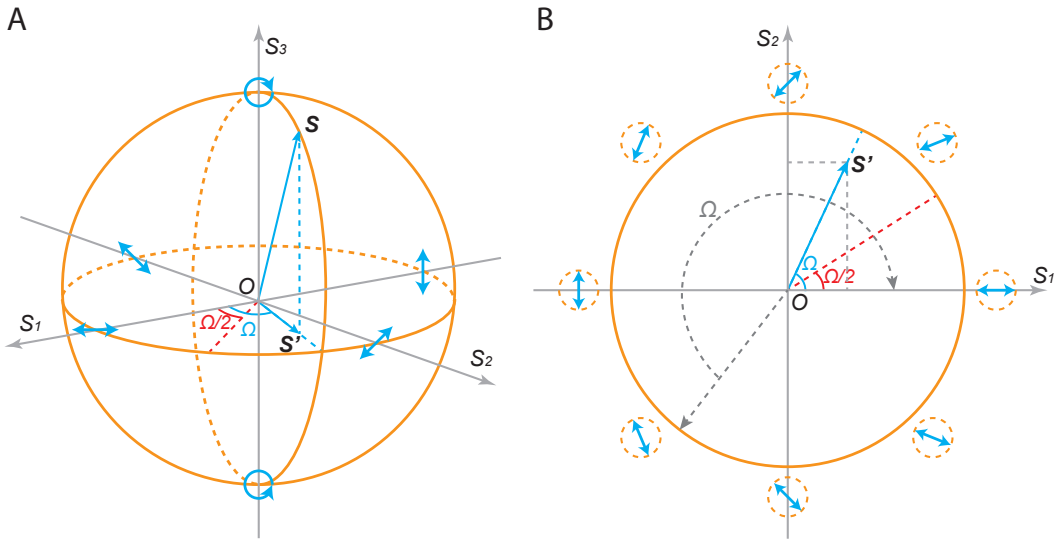

Figure S6: Poincare sphere and the Stokes' vector. (A) A general Stokes' vector $\vec{S}$ shown in the Poincare sphere. (B) Projection of $\vec{S}$ vector in sub-plane (s_1, s_2) and the definition of azimuth angle $\Omega/2$.

As we stated in the main-text, the polarization of the far-field radiation can be described by the Stokes' vector, which only depends on the right vector $|\Psi_n\rangle$. A general polarization state can be mapped to a vector pointing to an arbitrary direction in the Poincare sphere (blue vector denoted by $\vec{S} = [s_1, s_2, s_3]^T$, Fig. S6A). Specfically, the linear-polarized states (LPs) reside on the equatorial plane while the CPs reside on the north and south poles. The origin point O of the sphere corresponds to the amplitude vortex such as BICs. As shown in Fig. S6B, by projecting the $\vec{S}$ vector in the equatorial plane of the sphere, a sub-vector $\vec{S}'$ can be obtained. The angle Ω between $\vec{S}'$ and the s_1 axis is two times of the azimuth of the polarization ellipse. In literature, polarization topological charge is commonly used for depicting the radiation geometry, defined as the winding number of the azimuth. According to Fig. S6B, the polarization topological charge is exactly half of the winding number of the $\vec{S}'$ vector in sub-plane (s_1, s_2).

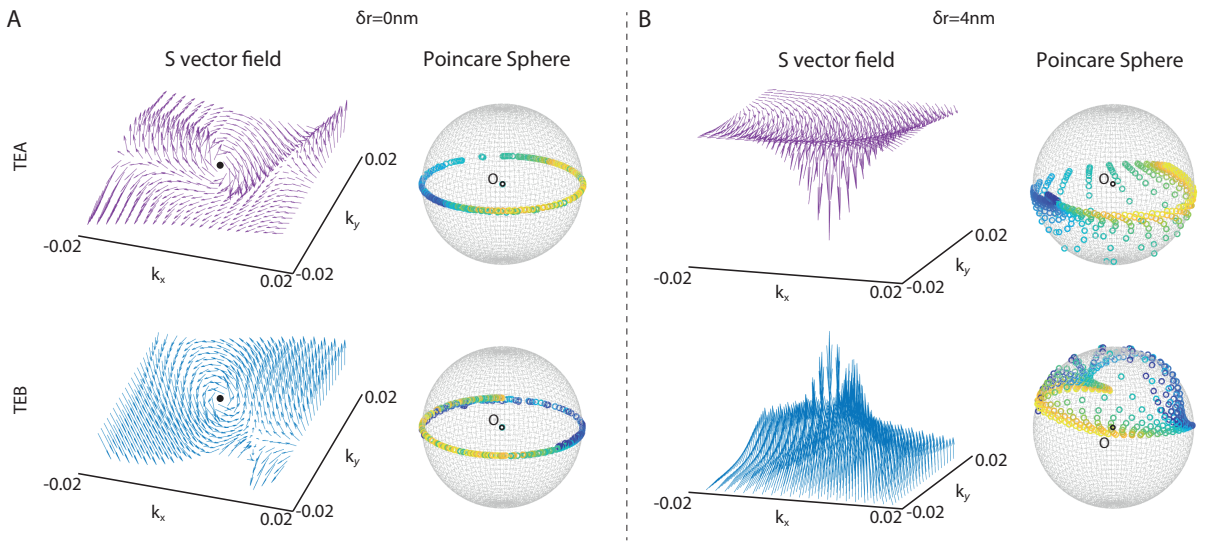

Figure S7: Radiation geometry of the PhC slab shown in Fig. 2 in the main-text. (A) $\vec{S}$ vector vortexes in momentum space and the corresponding ring-like distribution in the Poincare sphere for PhC of $\delta_r = 0$. (B) Anti-meron-like/meron-like configurations in momentum space and corresponding semi-sphere-like distribution in Poincare sphere for PhC of $\delta_r = 4$ nm.

To investigate the radiation geometry of the PhC slab we discussed in the main-text, we reproduce the polarization fields shown in Fig. 2E and F in the main-text, by plotting the $\vec{S}$ vector fields from channel C_3 (Fig. S7). First, we consider the case that $\delta_r = 0$ supports a DP at $\mathcal{K}_1$ point, where the far-field polarization can't be well-defined for both $TE_{A,B}$ modes. As shown in left panels of Fig. S7A reproduced from Fig. 2E in the main-text, vortexes of $\vec{S}$ around the DP (black dot) can be found for both $TE_{A,B}$ bands. According to Fig. S6, such $\vec{S}$ vortexes result in windings in the azimuth of the polarization ellipse, giving rise to half-integer topological charges of $q = 1/2$ for both $TE_{A,B}$ bands. In other words, the nonzero half charges shown in Fig. 2E are exactly the projection of $\vec{S}$ vortexes, as the footprints of the DP in the far-field radiation, not the consequences of CPs. Further, we map the $\vec{S}$ vector fields into the Poincare sphere, (right panels, Fig. S7A). For both $TE_{A,B}$ bands, the distribution of polarization shows as ring-like strips around the equator, confirming that there exist no CPs.

Next, we consider nonzero $\delta_r = 4$nm to lift the DP. The $\vec{S}$ vectors from channel C_3 for both $TE_{A,B}$ bands are shown in the left panels of Fig. S7B, reproduced from Fig. 2F. Compared to the $\vec{S}$ vortexes in Fig. S7A, the configuration of $\vec{S}$ vector fields changes abruptly: anti-meron-like and mero-like features are found for $TE_{A,B}$ bands, respectively, with left- and right-handed CPs emerging near the $\mathcal{K}_1$ point. The meron-like/anti-

meron-like configurations can be verified by our experiment results shown in Fig. 3E in the main-text. Similarly, we map the $\vec{S}$ vector fields into the Poincare sphere, showing two hemisphere-like distributions that cover the south and north poles, respectively. The hemisphere-like features confirm the existence of anti-meron-like and meron-like geometric structures, indicating the half-charges in Fig. 2F and 3E in the main-text are carried by the CPs.

Fig. S7 explains the origins of the meron-like/anti-meron-like geometry in far-field radiation. In brief, the DP creates vortexes on the $\vec{S}$ vector fields for both $\mathrm{TE}_{A,B}$ bands. When the DP is lifted by a nonzero δ_r, the $\vec{S}$ vortexes abruptly degrade to anti-meron for TE_A mode and meron for TE_B accordingly. The non-trivial radiation geometry can be characterized by the "Skyrmion number"[8–10] defined as:

$$Q = \frac{1}{4\pi}\oint \vec{S}\cdot(\partial_{k_x}\vec{S} - \partial_{k_y}\vec{S})ds \tag{S27}$$

which characterizes the solid angle of the swirling configuration of $\vec{S}$ vector in the Poincare sphere. For example, for $\vec{S}$ vortexes shown in Fig. S7A, the Skyrmion numbers of the ring-like strip structures are zero for both two bands. Instead, in Fig. S7B, the Skyrmion number is $Q = \pm 1/2$ for meron-like and anti-meron-like features, respectively. When splitting the DP, the phase transition happens as the zero Skyrmion numbers carried by $\vec{S}$ vortexes split into a pair of Skyrmion numbers of $Q = \pm 1/2$, located in two separate bands. During the phase transition, the total Skyrmion number of this two-level system is conserved to be zero: $Q_{all} = 0 + 0 = 1/2 - 1/2$.

We emphasize that the conventional polarization topological charges also conserve during the transition. The topological charges describe the geometry of $\vec{S}'$ in sub-plane (s_1, s_2) (Fig. S6), not the winding structure in 3D Poincare sphere which should be depicted by the Skyrmion number instead. Projecting the $\vec{S}$ vortexes (left panels, Fig. S7A) and meron-like/anti-meron-like features (right panels, Fig. S7B) into sub-plane (s_1, s_2) would create the same topological half-charges of $q = 1/2$. In other words, the topological charges are unchanged during the phase transition and thus cannot manifest the transition. This can be verified by Fig. 2E and F. It also indicates that different $\vec{S}$ configurations may result in the same topological charges.

Another equivalent definition of Skyrmion number can be derived as:

$$\begin{aligned} Q &= \frac{1}{4\pi}\oint \vec{S}\cdot(\partial_{k_x}\vec{S} - \partial_{k_y}\vec{S})ds \\ &= -\frac{1}{2}\oint i\nabla_{\mathbf{k}_\parallel}\times\langle\Psi(\mathbf{k}_\parallel)|\nabla_{\mathbf{k}_\parallel}\Psi(\mathbf{k}_\parallel)\rangle ds = -\frac{1}{2}B^r_{rr} \end{aligned} \tag{S28}$$

Eq. S28 shows that the Skyrmion number can be calculated from the integral on the "right-right" curvature $B^r_{rr} = i\nabla_{\mathbf{k}_\parallel} \times \langle \Psi(\mathbf{k}_\parallel) | \nabla_{\mathbf{k}_\parallel} \Psi(\mathbf{k}_\parallel) \rangle$ depending on the right vector $|\Psi\rangle$ only. In fact, the Skyrmion number and "right-right" curvature directly correspond to the PB phase of the radiative vector $|\Psi\rangle$ in momentum space, and thus characterize the radiation geometry only.

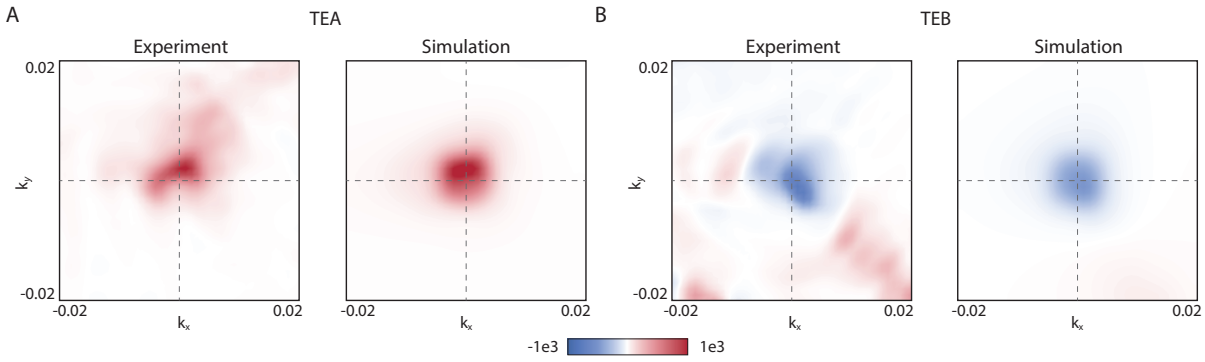

Figure S8: Measured and simulated "right-right" curvatures for PhC with $\delta_r = 4$nm. (A) The measured (left panel) and simulated (right panel) "right-right" curvatures for TE_A mode. (B) The measured (left panel) and simulated (right panel) "right-right" curvatures for TE_B mode.

We present an example of "right-right" curvatures in Fig. S8. We consider a PhC sample with $\delta_r = 4$ nm and measure the "right-right" curvature for both TE_A and TE_B bands. Compared to the radiation Berry curvature ("left-right" curvature) in Fig. 4 in the main-text, the "right-right" curvature shows distinct features. First, the "left-right" curvature of two-level bands are constrained by the bi-orthogonality condition which involves both two bands. As a result, they hold opposite signs but the same absolute value. Even with taking the third TE_C band into account, their absolute values are still very close to each other, verified by our simulation and experiment results. However, since the "right-right" curvature only depicts the radiation geometry of one band, it has no direct dependency on another band. We find that for different bands, they have different shapes and values of the "right-right" curvature: the peak absolute value for TE_A band is significantly larger than that for TE_B band. Second, the "left-right" curvature corresponds to the bulk topology originated from the split DP. Therefore its peak value always locates at the $\mathcal{K}_1$ point. As a comparison, the "right-right" curvature only depict the radiation geometry, and its peak value pins at the location of CPs. By increasing δ_r, the band gap becomes wider, and thus the CPs gradually deviate from the $\mathcal{K}_1$ point, and so do the peak values of "right-right" curvatures. As shown in Fig. S8, the peak values of "right-right" curvatures of TE_A and TE_B slightly deviate from $\mathcal{K}_1$ point upward and downward, respectively.

1. Liang, Y., Peng, C., Sakai, K., Iwahashi, S. & Noda, S. Three-dimensional coupled-wave model for square-lattice photonic crystal lasers with transverse electric polarization: A general approach. *Phys. Rev. B* **84**, 195119 (2011).

2. Peng, C., Liang, Y., Sakai, K., Iwahashi, S. & Noda, S. Three-dimensional coupled-wave theory analysis of a centered-rectangular lattice photonic crystal laser with a transverse-electric-like mode. *Phys. Rev. B* **86**, 035108 (2012).

3. Yang, Y., Peng, C., Liang, Y., Li, Z. & Noda, S. Analytical perspective for bound states in the continuum in photonic crystal slabs. *Phys. Rev. Lett.* **113**, 037401 (2014).

4. Zhen, B., Hsu, C. W., Lu, L., Stone, A. D. & Soljačić, M. Topological nature of optical bound states in the continuum. *Phys. Rev. Lett.* **113**, 257401 (2014).

5. Joannopoulos, J. D., Johnson, S. G., Winn, J. N. & Meade, R. D. Molding the flow of light. *Princet. Univ. Press. Princeton, NJ [ua]* (2008).

6. Asbóth, J. K., Oroszlány, L. & Pályi, A. A short course on topological insulators. *Lecture notes in physics* **919**, 166 (2016).

7. Shen, H., Zhen, B. & Fu, L. Topological band theory for non-hermitian hamiltonians. *Phys. Rev. Lett.* **120**, 146402 (2018).

8. Skyrme, T. Particle states of a quantized meson field. *Proc. Math. Phys. Eng.* **262**, 237–245 (1961).

9. Skyrme, T. H. R. A unified field theory of mesons and baryons. *Nucl. Phys.* **31**, 556–569 (1962).

10. Fert, A., Reyren, N. & Cros, V. Magnetic skyrmions: advances in physics and potential applications. *Nat. Rev. Mat.* **2**, 1–15 (2017).